Journal of Molecular Liquids 386 (2023) 122451

Contents lists available at ScienceDirect

Journal of Molecular Liquids

journal homepage: www.elsevier.com/locate/molliq

Heterogenity of graphite oxide particles obtained with wet oxidative exfoliation

Shereen Farah [a], Benjámin Gyarmati [a], János Madarász [b], Silvia Villar-Rodil [c], Juan M.D. Tascón [c], Krisztina László [a,*]

[a] Department of Physical Chemistry and Materials Science, Faculty of Chemical Technology and Biotechnology, Budapest University of Technology and Economics, Műegyetem Rkp. 3, H-1111 Budapest, Hungary
[b] Department of Inorganic and Analytical Chemistry, Faculty of Chemical Technology and Biotechnology, Budapest University of Technology and Economics, Műegyetem Rkp. 3, H-1111 Budapest, Hungary
[c] Instituto de Ciencia y Tecnología del Carbono, INCAR-CSIC, Francisco. Pintado Fe 26, 33011 Oviedo, Spain

ARTICLE INFO

Keywords:
Graphene oxide
Centrifugation
Fractionation
Morphology
Surface chemistry
Hydration
Viscosity

ABSTRACT

Wet oxidative exfoliation of graphite is one of the most frequently applied techniques to obtain aqueous dispersions of hydrophilic graphene derivatives as required, e.g., in 3D printing, wet spinning or film casting. Due to the harsh conditions of the process, the resulting suspension is a mixture of particles with a wide distribution range both of physical dimensions and chemical properties. An aqueous graphite oxide suspension was obtained by an improved Hummers method and separated into five fractions by controlled centrifugation. The fractions were characterized and compared by various methods, revealing their diversity in size, chemical properties and application-related viscosity. The characterization methods (powder XRD, Raman spectroscopy, ATR-FTIR spectroscopy, XPS, potentiometric titration, rheology) exhibited subtle but measurable differences that exceeded the standard deviation of the techniques employed, but no systematic trend was found across the fractions in any of the properties investigated. The conditions of our centrifugal separation hardly meet the constrains of the ideal of Stokes's law, the polydispersity of the high aspect ratio particles as well as their concentration close to the percolation limit challenge the independent sedimentation of the platelets.

1. Introduction

The wet oxidative exfoliation of graphite is still one of the most frequently applied techniques to obtain its 2D oxidized derivatives, multilayer graphite oxide [1–3] or few or monolayer graphene oxide [4], although the distinction is often misused in the literature [5]. The type (natural or synthetic) the size and shape of the precursor graphite particles [6,7], the exfoliation route [4] and the subsequent purification process [8] rank among the essential factors that determine the overall properties of the oxidized product. The macroscale performance of the suspensions is governed by the physico-chemical properties of the primary particles, defining their particle–particle and particle–solvent interactions [9–15]. The nanoparticles obtained often preserve structural defects, e.g., dislocations [16] or vacancies inherited from the parent graphite. Due to the harsh conditions of the oxidative wet exfoliation methods, the resulting suspension consists of highly heterogeneous platelets with a wide distribution of dimensions both in the layer planes and in the crystallographic *c*-axis. The particles also possess a diversity of layer numbers, aspect ratios and surface chemistry [17]. The latter involves the ratio of partly saturated and aromatic regions, carbon vacancies as well as oxygen functionalities distributed along the basal plane and along the edges with a wide variety both in quality and concentration [18].

Sonication, chemical or thermal post-exfoliation treatments may narrow the distribution range of the various characteristics, but these methods can also have detrimental effects on the size, integrity, oxidation state, etc. [19–21]. Long and excessive sonication as well as oxidative procedures result in a decrease in lateral dimensions of the platelets [19,22,23] or formation of new defects (small holes) in the sheets [22,23].

The continuous increase in application potential of graphite oxide and graphene oxide requires particles of well-defined properties. A wide variety of chemical and/or physical approaches have been studied for size fractionation of the flakes, including pH-sedimentation [9], salting-out [24], solvent selective sedimentation [11], oil-in-water emulsion separation [13], spherical particle adhesion [25], filtration [10],

* Corresponding author.

https://doi.org/10.1016/j.molliq.2023.122451
Received 3 March 2023; Received in revised form 22 June 2023; Accepted 26 June 2023
Available online 28 June 2023

controlled directional freezing [14], electrophoresis [26–29] or centrifugation [15,30–34].

In principle, centrifugation seems to be a simple and scalable method for separating particles in suspension according to their size, shape, and density [35–37]. Nevertheless, the efficiency is strongly affected by the viscosity of the medium and the rotor speed and the technique is time and energy consuming.

Traditionally, the sedimentation rate of colloidal particles relies on Stokes's law and can be expressed as

$$v_s = \frac{d^2 \cdot (\rho_p - \rho_m) \cdot \omega^2 \cdot r}{18 \cdot \eta} \quad (1)$$

where v_s is the velocity of sedimentation in centrifugal field; d is the diameter of the spherical particle, ρ_p and ρ_m are the density of the dispersed particle and dispersion medium, respectively; ω is the angular velocity of centrifuge, r is radius from axis of rotation; and η is the dynamic viscosity of the dispersion medium [38,39].

Assorted versions of the technique have also been applied to obtain graphene oxide suspensions of particles with narrow size distribution (Table 1). The medium most often used is pure water [15,30] or various aqueous solutions [31–33]. In the differential centrifugation, a single solvent is employed with different centrifugal forces to separate the particles: Yue *et al.* separated 2 μm and 350 nm graphene oxide fractions by applying centrifugal fields of 100–200 g and 10,000 – 30,000 g from an aqueous suspension obtained by a modified Hummers method [30]. Density gradient centrifugation applies a fixed centrifugal force, in which the gradient is set by tuning the medium density with glycerol or sucrose in various concentrations [32,34]. The drawback of this method is that an additional purification step is required. Surface modification with thermoresponsive recyclable poly-(N-isopropylacrylamide) was found to amplify the difference between the graphene oxide particles of different sizes, thus improving the separation efficiency [15].

As mentioned above the exfoliated particles are heterogeneous in their physical dimensions and chemical features. Our aim was to reveal the range of these differences. An aqueous suspension of graphite oxide (GO) was obtained from natural graphite with an improved Hummers method [4]. Without any further treatment the as-prepared particles were separated into five fractions by controlled centrifugation according to the method of Coleman's group [35] developed for graphene flakes. The fractions and the parent GO were characterized and compared by a wide range of methods revealing their diversity in size, chemistry and rheological properties. The techniques employed included powder X-ray diffraction (XRD), Raman spectroscopy, attenuated total reflectance Fourier transform infrared spectroscopy (ATR-FTIR), X-ray photoelectron spectroscopy (XPS), potentiometric titration and rheology.

Table 1
Various centrifugation methods applied for wet graphene oxide/graphite oxide separation.

Method	Centrifugation conditions	Concentration (mg mL^{-1})	Medium	Particle sizes	Comments	Ref.
Differential centrifugation	250, 2000 and 4000 rpm, 10 min.	2	Aqueous	Pristine: 1—400 μm^2 Fractions: 0–35 μm^2 0–200 μm^2 0–500 μm^2 Thickness: 0.99 nm, 0.96 nm, 0.91 nm Method: SEM and AFM	Reversible adsorption of poly(N-isopropylacrylamide); additional temperature modulation needed	[15]
	100–200 g and 10000–30000 g	NA*	Aqueous	Lateral: 2 μm and 350 nm Thickness: 3.9 and 4.05 nm Method: AFM		[30]
	2720 rpm, 10 min; 6800 rpm, 10 min,; 8000 rpm, 20 min	1	pH 9, 10 mM KCl	Pristine:150–1500 nm Fractions: 40–500 nm 50–3000 nm 700–4000 nm Thickness: 1 nm for 1st and 2nd; 100–150 nm for 3rd step Method: DLS	Additional purification required	[31]
Density gradient centrifugation	8000 g, 3 h	0.01	Aq. glycerol (50–5%)	Fractions: 145–155 nm 345–355 nm 500–700 nm 800–1000 nm Thickness: 1.1 ± 0.2 nm Method: DLS and AFM	Narrow size distribution; low yield due to low initial concentration	[32]
	50000 rpm, 2.5 h	NA*	Aq. iodixanol, (5–20%)	Pristine: 10–300 nm Functionalized: 20 nm Fractions: 2–10 nm 2–18 nm 10–22 nm Thickness: 1 nm Method: AFM	Narrow size distribution; additional purification required	[33]
	50000 rpm, 5 min	NA*	Aq. sucrose (20:66%)	Fractions: 10–60 nm 18–150 nm 100–560 nm 150–560 nm 70–560 nm Thickness: 0.7 nm Method: AFM	Additional purification required	[34]

* NA: not available.

2. Materials and methods

Graphite oxide (GO) was obtained from natural graphite (Graphite Týn, Týn nad Vltavou, Czech Republic; carbon content min. 99.5%, only 10% of the particles exceeds 0.063 mm) by an improved Hummers method [4]. The concentration of the obtained suspension and the yield were 11.2 mg mL^{-1} and 80%, respectively. The aqueous GO suspension was stored in a dark glass bottle at ambient temperature. Freeze-dried samples obtained from the suspension were stored in a desiccator over silica gel.

2.1. Fractionation of the GO suspension

The particles were separated by centrifugation (Jouan BR4i Multifunction Centrifuge, Thermo Scientific, USA) at 25 °C. After mild ultrasonication (300 W, 45 kHz, 15 min) the.

1.12 mg mL^{-1} aqueous GO suspension was centrifuged at 15,100 g for 30 min. The supernatant was separated and the gel-like GO sediment was re-dispersed with water prior to the further centrifugation steps at 10,700 g, 7000 g, 4200 g, and finally at 2000 g. The supernatants were concentrated in an additional centrifugation step at 15,100 g. The scheme of the separation process is illustrated in Fig. 1. The concentrated gel-like GO1–GO5 samples (ca 9.5 mg mL^{-1}) were stored and freeze-dried in the same way as the parent sample.

2.2. Characterisation methods

The crystalline structure of samples with similar thickness was investigated by an X'pert Pro (PANanalytical Bv, The Netherlands) powder X-ray diffractometer with monochromatic Cu K_α radiation (λ = 1.5406 Å). Results were analyzed by X'pert High Score software. The interlayer spacing d of the lattices was obtained from Bragg's law [40],

$$n\cdot\lambda = 2\cdot d\cdot sin\theta \quad (2)$$

n is the diffraction series integer 1, 2, …. etc. λ is the wavelength of the used X-ray and θ is the Bragg's angle of the plane. 2θ was determined with ± 0.2. The *002* peak around $2\theta \approx 11.5°$ was used for the analysis. The stacking height (L_c) was calculated from the Scherrer formula [41],

$$L_c = \frac{K\cdot\lambda}{FWHM\cdot cos\theta} \quad (3)$$

The shape factor $K = 0.93$ [42], and *FWHM* (in radian) stands for the full width of the 002 peak at half maximum. The number of layers N_c was estimated as L_c/d.

Raman spectra were recorded with a LabRAM (Horiba Jobin Yvon) instrument (λ = 532 nm Nd-YAG laser source, 15 mW power in the focus point). The freeze-dried GO samples were measured at three different spots, using a filter of 0.6 OD to reduce the intensity of the excitation beam. LabSpec 5 software was applied for parameter optimization and data collection. The first and second-order regions of the baseline corrected spectra were deconvoluted to Lorentzian functions with the conventional fitting procedure of the Origin Pro 9 program. The average size of the aromatic clusters (L_a in nm) was estimated from the Tuinstra-Koenig-Cançado expression [43],

$$L_a = \frac{2.4\cdot10^{-10}\cdot\lambda^4}{(I_D/I_G)} \quad (4)$$

λ (in nm) is the wavelength of the laser source and I_D/I_G is the intensity ratio of the D and G bands.

The FTIR spectra of the freeze-dried samples were recorded on a Bruker SpecAC Tenzor 37 attenuated total reflection Fourier transform infrared (ATR-FTIR) spectrophotometer (Golden Gate type with Diamond Head -Golden Gate™ Single Reflection Diamond ATR System).

X-ray photoelectron spectroscopy (XPS) was performed on a SPECS system equipped with Phoibos 100 hemispherical electron energy analyzer. The freeze-dried cotton-like, bulky aerogel lumps (Figure S1 in the Supplementary Material) were fixed to the XPS sample-holder with double-sided carbon adhesive tabs. They were compressed to form a ≥ 0.2 mm thick layer on the carbon adhesive. The spectra were acquired at pressure below 10^{-7} Pa using a monochromatic Al X-ray source operated at 14.00 kV and power of 175 W. The photoelectrons were analyzed at a take-off angle of 90° and in constant pass energy mode, using pass

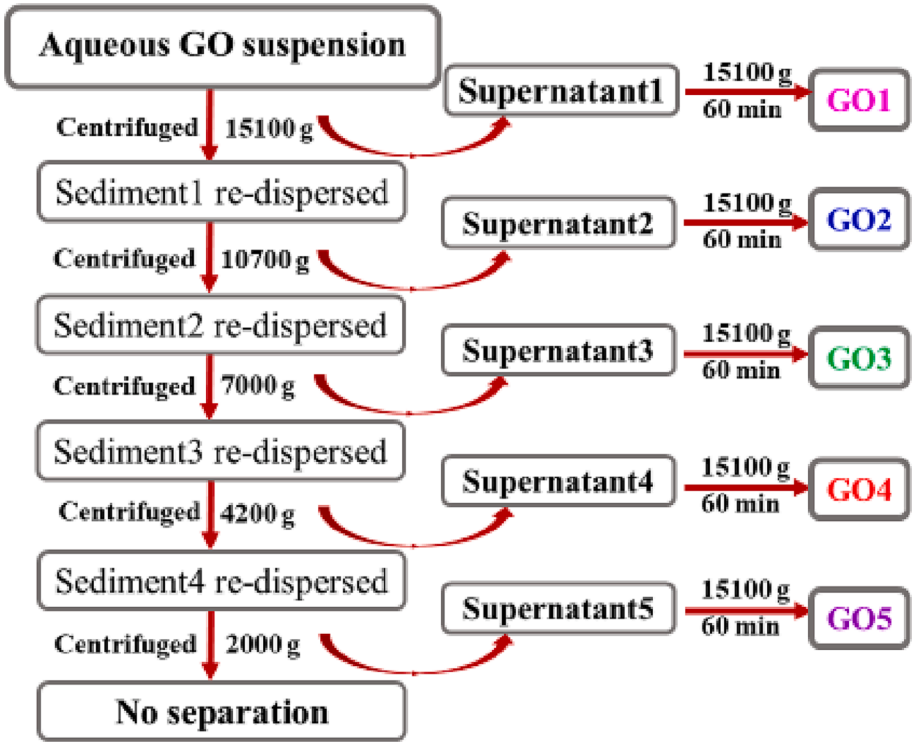

Fig. 1. Diagram of the fractionation process. The GO1 - GO5 sediment samples were analyzed.

energy of 50 eV for the survey spectra and 10 eV for the high-resolution core level spectra. The surface charging effect was counteracted by the use of an electron flood gun. CasaXPS software was used for data processing. Core level curve fitting was performed using a Shirley background and a standard least squares algorithm. Gaussian and Lorentzian functions (80:20) were used for the deconvolution.

The potentiometric acid-base titrations were performed at 23 ± 1 °C under CO_2 free conditions maintained by constant N_2 gas flow. 50 mg GO suspended in 50 mL 0.1 M KCl solution was titrated in the pH range ~3 to ~10, using an auto-titrator (Metrohm 808 Titrando, Tiamo, version 1.2) adjusted to deliver automatic additions of 0.1 M NaOH and 0.1 M HCl solutions (both in 0.1 M KCl). The stability criterion between successive additions was 1 mV min^{-1}. Between stable pH readings a 60 s delay was allowed before the next volume was added. The single-junction glass pH electrode (Metrohm, pH range: 1–13, filled with 3 M KCl) was calibrated using commercial pH buffers (Merck, Certipur® buffer solutions) with pH = 4.00, 6.00, and 9.00). The net proton surface excess n^{σ} related to the unit mass of solid was determined from the initial ($c_{i,0}$) and the equilibrium ($c_{i,eq}$) concentrations [44]

$$n^{\sigma} = \frac{V \cdot (c_{i,o} - c_{i,eq})}{m} \quad (5)$$

where V is volume of the liquid phase and m is the mass of the GO. Titrations were performed in triplicates. The concentration of the titrated surface groups was calculated as the difference of the n^{σ} values in the corresponding low and high pH end points. The pK_a distributions were derived by the SAIEUS procedure [45,46].

Atomic force microscopic images were taken with a Nanosurf Flex-AFM atomic force microscopy system (Nanosurf, Liestal, Switzerland) under air, in dynamic mode utilizing Budgetsensors Tap150GD cantilevers (BudgetSensors, Sofia, Bulgaria). 100 μL 1000-fold diluted aqueous samples were deposited on the previously cleaned silicon wafers and distributed by spin-coating at 4000 rpm, then dried in vacuum. Images were collected at randomly selected locations and processed using the Gwyddion software [47].

A Malvern Zetasizer Pro-Blue (Malvern Instruments) was applied to obtain both the particle size distribution (PSD) and the zeta potential of the samples. [GO fractions were diluted with Millipore water to 20 mg/L, and sonicated for 5 min prior to the measurements. The calculation for PSD was performed by assuming spherical geometry. The refractive index used for the calculations was 1.957 [48]. The Helmholtz - Smoluchowski equation was used to convert the electrophoretic mobility values into the zeta potential. The measurements were controlled and evaluated by ZS XPLORER software.

Flow and viscosity curves of ca 9.5 mg mL^{-1} (~0.7 *v/v*% taking the real density of graphene oxide of 1.39 g cm^{-3} [49]) GO samples were recorded in rotational mode on Anton Paar Physica MCR 301 (Austria) rheometer. A pre-shear of 100 s^{-1} was applied for 30 s, then the shear rate was varied from 10^{-2} s^{-1} with 5 data points in each decade. Each point was recorded for 10 s. The shear stress and the viscosity were monitored as a function of shear rate. All data were acquired by using a 25 mm diameter parallel plate PP25-SN50981 arrangement and plate gap of 0.3 mm at constant temperature of 25 ± 0.01 °C. For each measurement, about 0.5 mL aqueous suspension was used. All experiments were conducted in a triplicate. Rheoplus software was used for data analysis, and figures are plotted on a logarithmic scale.

3. Results

3.1. Morphology and texture of the fractions

The AFM image and size distribution curves from DLS measurements in Fig. 2 reveal the dimensional heterogeneity of the parent GO particles prior to their separation. The systematic shift of the successive distribution curves (Fig. 2**b**) show the instability of the sample. The time between consecutive parallel measurements on the same sample was about 5 min, therefore, the shift of the particle size distribution curves might be attributed to aggregation. Indeed, the corresponding zeta potential (shown later in Fig. 7**c**) indicates the incipient colloidal stability of this suspension [50]. The polydispersity index (≥0.5) also designates the poor quality of the correlation functions and the uncertainty of the particle size distribution results [51,52].

The repeated re-dilution in the successive centrifugation steps reduced the initial concentration of the suspensions from 1.12 mg mL^{-1} to 0.85, 0.55, 0.25 and 0.07 mg mL^{-1}. **Figure S2** shows the mass distribution of the GO particles in the five fractions. It should be expected that GO1 contains the particles of the lowest density, while GO5 contains those of the highest density. **Figure S3** presents the PSD of the fractions.

The X-ray diffractograms of the freeze-dried samples and the structural parameters deduced from them are shown in Fig. 3**a**. The expected sharp peak in the interval of 2Θ = 11.1–11.5° assigned to the (*002*) crystalline plane was observed in all the fractions. Both the peak positions and the FWHM values show minor, but not systematic changes (**Table S1**). The oxygen containing functional groups weaken the interaction between the adjacent layers, therefore the extended *d* spacings of the fractions (Fig. 3**b**) reflect an increased degree of oxidation [4]. It is also affected by the water molecules confined in the

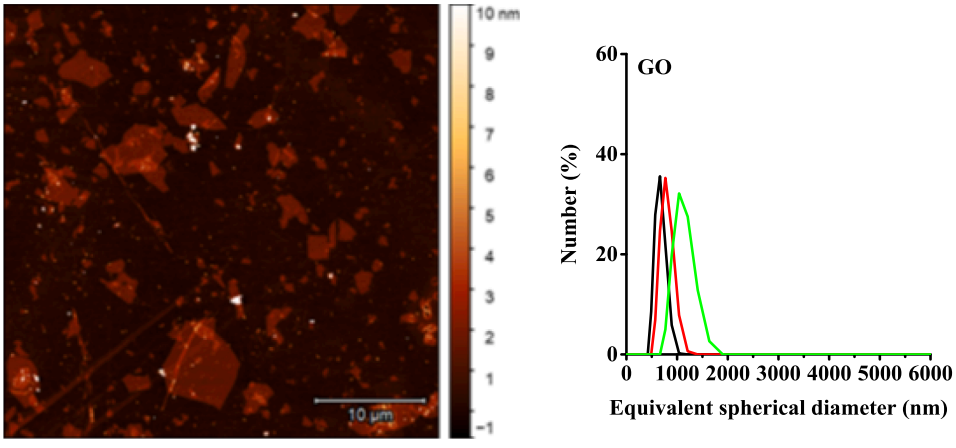

Fig. 2. AFM image (a) and particle size distribution curves of the parent GO sample. Black, red and green curves belong to three consecutive parallel measurements on the same sample (b).

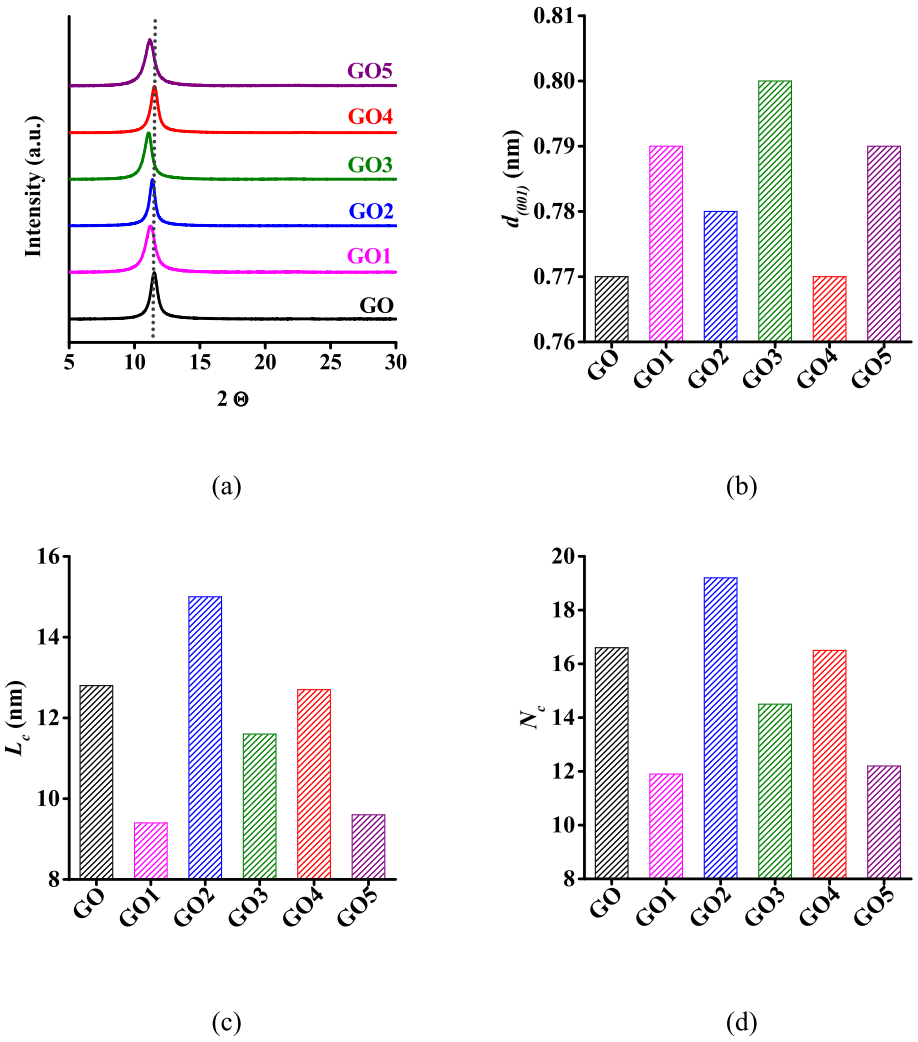

Fig. 3. Powder XRD diffractograms (a), *d*-spacing (b), stacking height L_c (c) and number of layers N_c (d) of the GO samples.

interlamellar space of the graphene oxide particles either during the exfoliation or the storage [49,53]. Similarly, no systematic change is found either in the crystallite height L_c (Fig. 3**c**) or in the number of layers (Fig. 3**d**).

The Raman spectra of the freeze-dried samples were recorded in the 800–3500 cm^{-1} range (Fig. 4**a**). The first and second order regions were deconvoluted and assigned similarly as in our previous work [49,54]. The deconvolution of the as-prepared GO spectrum is shown in **Figure S4**, while the assignation of the characteristic Raman bands is summarized in **Table S2**. The fractionated samples practically have the

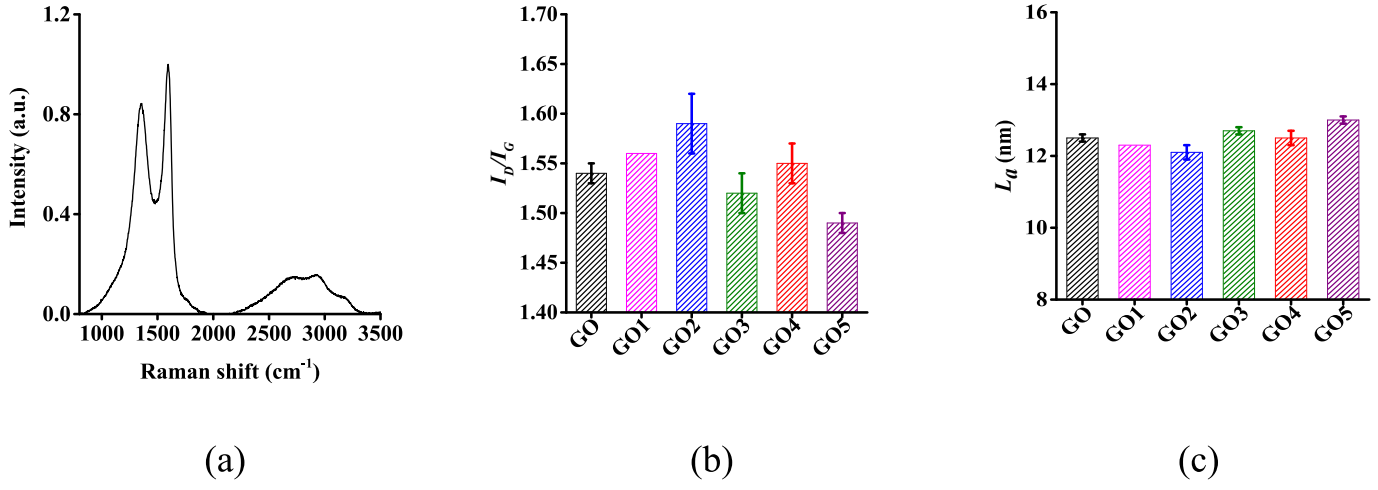

Fig. 4. Raman spectrum of the parent GO sample (a); I_D/I_G ratio (b) and Raman active lateral extension (L_a) from Eq. (3) (c) of freeze-dried GO fractions.

same D, G and D' positions. The G and 2D bands in a dry single-layer graphene sample appear at 1585 and 2679 cm^{-1}, correspondingly, and show red and blue shift, respectively with the increasing number of layers [55–57]. All our samples showed this phenomenon: 1574–1577 cm^{-1} for the G band and 2701–2714 cm^{-1} for the 2D band, confirming the multilayer nature of the fractions already revealed by XRD. The intensity ratio I_D/I_G is acknowledged as the measure of the defects in graphitic planes [58]. GO1, GO2 and GO4 have higher, while GO5 has the lowest I_D/I_G ratio (Fig. 4**b**), and likely, a lower overall degree of oxidation than the other GO samples.

The intensity ratio I_D/I_G also allows to estimate the average size of the aromatic clusters (L_a) in the graphene sheets (Eq. (3). GO3 and GO5 have the highest values, 12.7 and 13.0 nm, respectively (Fig. 4**c**), exceeding that of GO. This result suggests that larger conjugated aromatic domains exist in these samples. In conformity with the literature [15], the heaviest GO5 fraction contains the fewest defects and may have the lowest degree of oxidation.

3.2. Chemistry

FTIR analysis was applied to identify the oxygen functionalities in the particles (Fig. 5**a**). The FTIR spectra of all samples contain a broad band in the range of 3000–3700 cm^{-1} belongs to the characteristic νOH vibration, while the band at 1732 cm^{-1} corresponds to the νC=O stretching vibrations of the carbonyl and carboxyl groups. The band at 1620 cm^{-1} is assigned to νC=C (stretching modes of aromatic rings), and the one at 1376 cm^{-1} belongs to the δOH bending modes of phenol and OH groups in tertiary alcohols. The characteristic band at 1220 cm^{-1} emanates from the νC–OH stretching vibrations, while the band at 1057 cm^{-1} may arise from the νC–O–C asymmetric stretching of epoxide rings [59,60]. The same oxygen functionalities are present in all samples but their spatial distribution and concentration may vary.

Assuming a widely accepted structural model of graphite oxide, epoxide and hydroxyl groups decorate the basal planes, while the carbonyl and carboxyl groups can be found along the edges of the graphite oxide platelets [17]. In all the fractions the intensity ratio of the peaks at 1220 cm^{-1} and 1620 cm^{-1} (C—OH/C=C) (Fig. 5 **b**) is considerably smaller than the intensity ratio of the peaks at around 1732 cm^{-1} and 1620 cm^{-1} (C=O/C=C) and 1057 cm^{-1} and 1620 cm^{-1} (C—O—C/C=C). The two latter ratios lie in the sequence GO5 < GO3 < GO4 < GO2 ≈ GO1, while the intensity ratio of the ~1220 cm^{-1} and 1620 cm^{-1} (C—OH/C=C) (Fig. 5**b**) increased in the following order GO5 < GO3 < GO4 < GO1 < GO2. According to Chen *et al.* the intensity ratio C=O/C=C decreases with GO size [10].

It can be concluded that the relative concentration of C=O and C—O—C groups is higher in GO1 and GO2. Previous studies found that graphene oxide with smaller diameter is more oxidized [10,15,61]. The GO5 fraction has the lowest relative concentration of epoxide and hydroxide groups, consistently with the largest size of the aromatic clusters (L_a) obtained from Raman results.

The surface composition of GO samples was confirmed by XPS. The survey spectrum and the deconvoluted C1s region of the parent GO, as typical examples, are shown in Fig. 6**a and b** respectively**.** The C1s region of the fractions and the O1s core level spectra are displayed in **Figures S5 and S6**, respectively.

The O/C ratios (Fig. 6**c**) were calculated and used for semi-quantitative comparison with similar materials reported in the literature, as the O/C ratio might be unreliable due to the incomplete removal of water [4]. Except for GO2, there is a slightly decreasing trend concomitant with the increase of the expected density of the fractions. Smaller and more oxidized GO flakes form more stable colloidal systems than the larger and less hydrophilic ones. Although the outgassing applied prior to XPS is quite extensive, it is impossible to get completely dry GO samples [17], the trend seen in Fig. 6**c** is confirmed by that found from deconvolution of the C1s band, which probes only the carbon atoms in various chemical environment and is unaffected by retained H_2O molecules.

As noted earlier, according to one of the most accepted structural models GO consists of intact graphitic regions interspersed with sp^3-hybridized carbons decorated with hydroxyl and epoxide functional groups on both surfaces of the sheet and sp^2-hybridized carbons with carboxyl and carbonyl groups mostly along the edges of the sheets [17]. These intact graphitic regions must be isolated, without a percolation path for electrical conduction implied by the need of *in situ* charge compensation. To obtain a more quantitative picture about the graphitic carbon the C1s spectra were deconvoluted into four peaks assigned to graphitic carbon (P1, BE ~284.5 eV), carbon singly bonded to oxygen in epoxy and hydroxyl groups (P2, BE ~286.6 eV), carbon in carbonyl groups (P3, BE ~287.9 eV), and carbon in carboxyl groups (P4, BE ~288.9 eV) [62] (Fig. 6**b** and **Figure S7**). Fig. 6**d** compares the distribution of the different carbon species in the fractions. Except for GO2, the increase in graphitic content reflects the increasing fraction number. Thus, there is a difference, although subtle, in the surface chemistry of the fractions. Although it could be expected that the lighter flakes have a higher relative content of carboxyl and carbonyl groups, no such trend is in fact observed here, as internal edges are also present in the GO particles [62]. The P2/P1 ratio follows the expected inverse trend to that of the percentage of graphitic carbon (**Figure S5a**). As for the ratio of

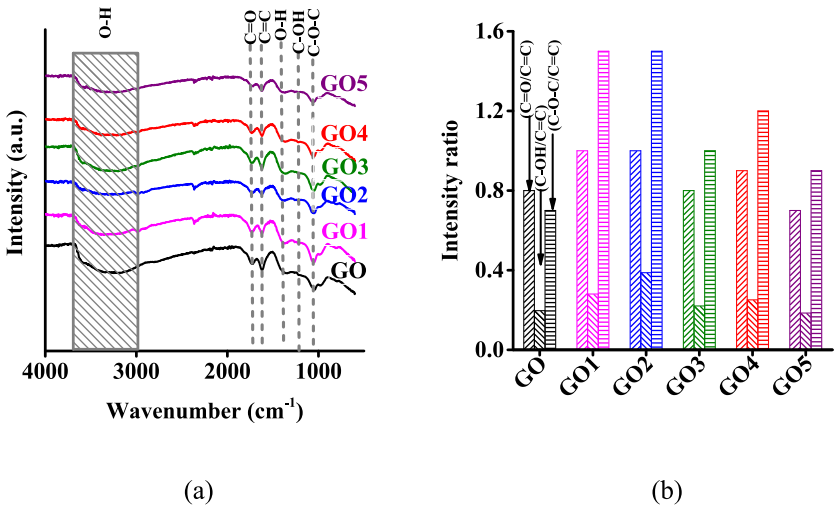

Fig. 5. FTIR spectra of freeze-dried GO samples. Spectra are vertically shifted for clarity (a). Intensity ratio of bands (C=O/C=C), (C—O—C/C=C) and (C—OH/C=C) of freeze-dried GO samples (b).

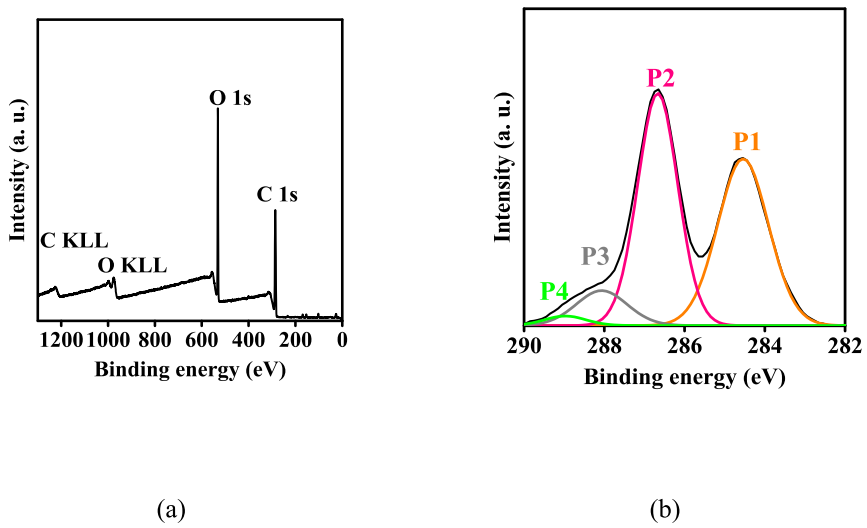

Fig. 6. XPS survey spectrum of GO (a) and deconvoluted C1s core level spectrum of parent GO (b): graphitic carbon, P1; carbon singly bonded to epoxy and phenolic hydroxyl groups (P2); double bonded carbon in carbonyl groups (P3); carbon in carboxyl groups (P4). O/C ratio of the freeze-dried GO samples (c) and distribution of the different C1s species (d) corresponding to the deconvoluted spectra in (c) and in Figure S5 of the Supplementary Material. The numerical data calculated from the XPS survey spectra the and high-resolution XPS core level deconvolution are respectively shown in Tables S3 and S4 of the Supplementary Material.

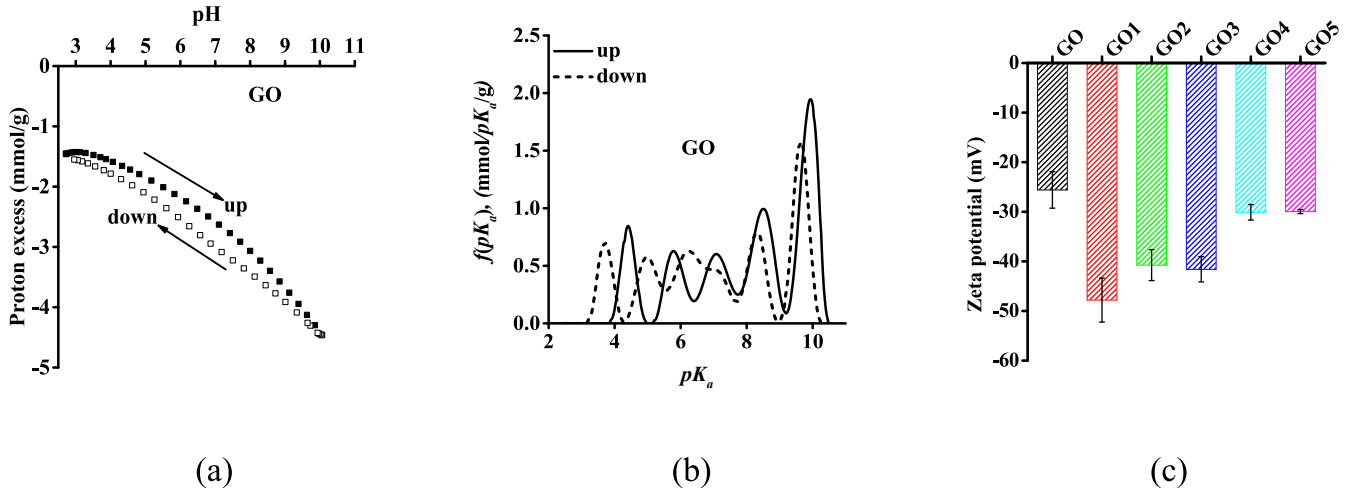

Fig. 7. Potentiometric titration curves (a); pK_a distribution curves of the surface oxygen groups in the parent GO (b); Zeta potential of GO samples (c).

carbonyl group to graphitic carbon (P3/P1) (Figure S5**b**), this quantity decreases as a function of increasing density fraction (including GO2). The ratio of carboxyl groups to graphitic carbon (P4/P1) (Figure S5**c**) is similar for all the samples. As expected, the observed differences are small, but are corroborated with FTIR and XRD results.

In view of the multitude of applications employing GO is in aqueous medium, the fractions were also characterized by potentiometric acid/base titration under CO_2-free conditions in the pH range 3–10. The

primary titration data were converted proton excess isotherms (Fig. 7**a, and Figure S8**). The titration was performed from pH 3 up to 10 (up) and back again to pH 3 (down). The reproducible hysteresis loop between the up and down datasets implies that the protonation occurring when the pH is gradually increased is irreversible.

The pK_a distribution curves of the surface oxygen groups were calculated with the SAIEUS program [45,46] and are shown in Fig. 7**b** and **Figure S9**. The overall concentration of the titrated groups was calculated as the difference of the end-points and is reported in Table 2.

The titration results also corroborate the recent GO model of Aliyev *et al.* [63]. They were able to identify lactone, quinone and ketone sites at the peripheral and defect areas of the graphitic sheet besides the oxygen functionalities proposed by Lerf and Klinowski [17].

The colloidal stability of the fractions was estimated from the zeta potential of the unbuffered aqueous suspensions with pH in the range 4.8–5.1. As expected from the potentiometric titration, the particles are negatively charged. The zeta potential of the fractions varies between −48 mV and −26 mV (Fig. 7 **c**) and follows the sequence of GO1 < GO2 ≈ GO3 < GO4 ≈ GO5. GO1, GO2 and GO3 have higher negative zeta potential, than the other samples. We recall that GO1 has the highest surface O/C ratio and the highest concentration of titrated functional groups. By contrast, the more extended particles in the GO4 and GO5 fractions have fewer defects and lower degree of oxidation.

Rheological properties of GO suspensions is of fundamental importance when GO is processed in aqueous dispersions, e.g., in 3D printing, wet spinning or film casting. As we have noted earlier, the microstructure of the concentrated GO–water colloid systems changes owing to the oxidative processes occurring in the suspensions during long-term storage [49]. The internal structure of the suspension is subject to a set of long and short-range forces, most of which (van der Waals forces, hydrogen bonding or electrostatic interactions) are related to the hydrophilic/hydrophobic properties of the particles, i.e., their surface chemical properties. The viscosity and flow curves of the various GO fractions having similar concentration are presented in Fig. 8. A pronounced shear-thinning behavior is observed in which the viscosity drops with increasing shear rate over the whole range of applied shear rate (Fig. 8**a**), while the flow curves clearly show the presence of a yield stress as a plateau at low shear rates (Fig. 8**b**).

On the basis of our earlier experience the measured data were fitted to the Herschel–Bulkley (HB) model, which combines the yield stress and the non-linear dependence of shear stress on shear rate and thus assumes non-Newtonian behavior above the yield stress (Eq. (6)) [64]

$$\tau = \tau_0 + k\cdot\dot{\gamma}^n \tag{6}$$

where τ is the shear stress $\dot{\gamma}$ is the shear rate, τ_0 is the steady shear yield stress, k is the consistency coefficient of the model, and n is the flow index ($0 < n < 1$). The fitting parameters were deduced from the plots in the shear rate range of 10^{-1} to 10^{2} s^{-1} (**Figure S10**). For isotropic liquids without long-term order, the value of n is close to 1, while shear-thinning liquids can be characterized with an n value below 1. In the present case the value of n lies in the interval of 0.35–0.50 (Fig. 9**a**). Such values confirm the non-Newtonian behavior of the systems. Higher yield stress (Fig. 9**b**) was observed for GO1 and GO5 with respect to other fractions that have approximately similar values. The rheological properties reveal the differences between the fractions but again no systematic trend is apparent.

Table 2
Total concentration of the titrated functional groups.

Sample	Concentration End	
	mmol g^{-1}	
	pH	
	upward	downward difference
GO	3.07	2.98
GO1	2.70	2.58
GO2	2.55	2.45
GO3	2.51	2.41
GO4	2.73	2.71
GO5	2.42	2.37

4. Discussion

Unlike reference works [15,30–34] no systematic trend was observed in the various properties studied along the fractions. It seems plausible that Stokes's law (Eq. (1)) is not applicable to our system, as this formula is valid for dilute suspensions of spherical, or even approximately spherical solid particles. In this context, dilute means independently settling particles in a medium having a viscosity that is equal to or very close to that of the dispersing medium.

One of the main factors is that the aspect ratio of the GO platelets in the present case is very far from that of a sphere, namely 1 [49]. Furthermore, the shape and the aspect ratio vary from particle to particle (see Fig. 2a in the Results section).

The GO particles are rich in hydrophilic functional groups (see FTIR and XPS spectra in Figs. 5 and 6, respectively, and their interpretation in the Results section) and their surface is therefore hydrated. The thickness of the sorbed water layer is influenced by the concentration of the functional groups along the edges of the platelets. The particles settle together with their hydrate shell with a rate determined by the extended hydrated size. Moreover, as revealed by the zeta potential values, not all the fractions contain particles with surface charge high enough to prevent particle coagulation. The effect of water on the density of the GO platelets must also be taken into consideration. As already noted, exfoliated GO particles possess structural defects inherited from the parent graphite, e.g., dislocations [16] or vacancies. The number of the imperfections proliferates further during the oxidation process: holes with multi-atomic size may be generated in the external layers of the platelets; the functional groups being formed during the oxidation locally expand the distance between the layers close to the edges. All these effects lead to the formation of nanocavities and extended layer spacing that can accommodate and intercalate the solvent. The separation of the particles is consequently governed by the density of the platelets with high water content rather than by the density of the "naked" GO particles themselves.

Last but not least, the viscosity of the dispersion medium should be addressed. The viscosity of pure water is 10^{-3} Pa·s at 20 °C and displays a Newtonian behavior which is evidently not the case for GO suspensions owing to their internal structure already at low particulate concentrations. The critical volume fraction ϕ_c at which the GO sheets already touch each other can occur in the range 0.1–1 *v/v* % [65–68] or equivalent to about 1–14 mg mL^{-1} [49]. Discrepancies in the value of the critical concentration and the viscosity is not surprising, since the aqueous GO systems studied by various research groups are intrinsically very different in several respects, including particle aspect ratio, size distribution or surface chemistry. In the present study the concentration (from 1.12 mg mL^{-1}, to 0.85, 0.55, 0.25 and 0.07 mg mL^{-1}) lies, except for the heaviest fraction, within the critical range, where the percolation threshold is achieved and the particles start to touch each other. At low shear rate, our measured viscosity of 9.5 mg mL^{-1} GO parent was 10^4 Pa·s which is comparable to that of Bai *et al.* [69] who measured this viscosity in the concentration range 1–9 mg mL^{-1}. The low concentration viscosity of their suspension is seven orders of magnitude higher than that of the pure solvent, thus confirming that the particles are not independent and the separation occurs within a structured medium.

The deviation of the expected systematic trend in the various properties can be explained by the imperfect separation. Nevertheless, the above discussed findings reveal that the particle size, the morphology and the surface chemistry of the GO platelets show surprisingly wide variations among the fractions. In some of the cases the differences are

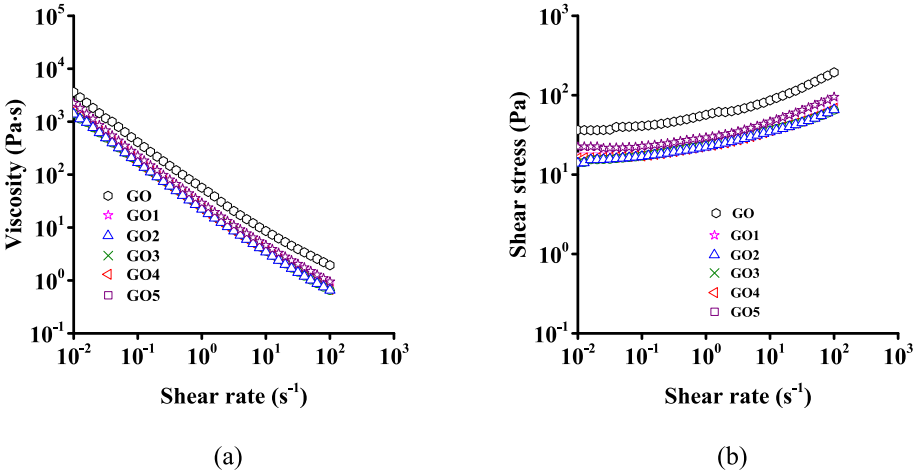

Fig. 8. Steady shear measurements on GO suspensions of different fractions. Effect of shear rate on viscosity (a) and shear stress (b).

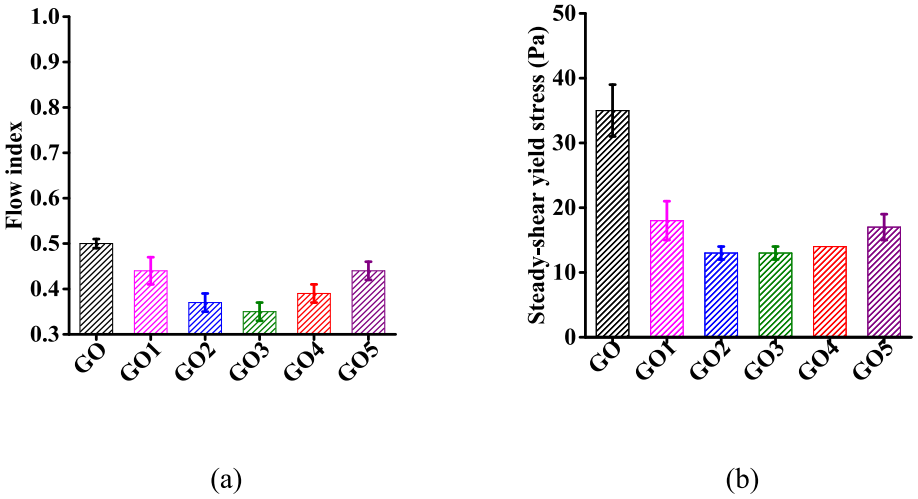

Fig. 9. Fitted parameters from the Herschel–Bulkley model. Flow index (a) and shear yield stress (b) of the GO samples.

subtle but exceed the experimental error of the methods applied.

5. Conclusions

GO particles obtained from natural graphite were separated into five fractions in aqueous media with centrifugation and the properties of the fractions were characterized by a wide range of methods to reveal the deviation of the various properties within the obtained suspended particles. The applied characterization methods showed that both the morphology and the chemistry of the GO platelets were heterogeneous. We revealed subtle but systematic differences exceeding the standard deviation of the applied methods. Despite the expectation, no systematic trend was found across the fractions in the dimensions, the number of layers, the defect concentration or the chemical composition along the fractions. This finding can be explained by the fact that the separation conditions did not meet the constrains of the Stokes's law introduced for the spontaneous sedimentation of fully independent solid spherical particles in a low viscosity medium where the particles get separated according to their mass. Practically none of these conditions holds here and viscosity itself shows a non-monotonic change complication the separation. Moreover, the defects and vacancies in the particles may lead to the formation of nanocavities ready to accommodate water molecules, modifying the density of the particles. This hydration is influenced by the concentration and distribution of the functional groups along the edges of the platelets. Consequently, the separation will be controlled by the density of the strongly hydrated platelets and not by the "naked" GO particles themselves resulting in non-systematic changes of the various properties across the fractions. The separation of the highly anisotropic 2D particles is therefore governed by the density of the strongly hydrated platelets, the network of which gives rise to a relatively high viscosity medium.

CRediT authorship contribution statement

Shereen Farah: Investigation, Writing – original draft. **Benjámin Gyarmati:** Methodology. **János Madarász:** Methodology. **Silvia Villar-Rodil:** Investigation, Writing – original draft. **Juan M.D. Tascón:** Methodology. **Krisztina László:** Conceptualization, Funding acquisition.

Declaration of Competing Interest

The authors declare that they have no known competing financial interests or personal relationships that could have appeared to influence the work reported in this paper.

Data availability

Data will be made available on request.

Acknowledgments

We extend our warm thanks to Bosznai, G. for his invaluable technical assistance. The SAIEUS software was kindly provided by Jacek Jagiello. We acknowledge the access to the instrumentation of the Soft Matter Group of our department and the Department of Organic Chemistry and Technology. We are thankful for the help of Attila Farkas, Gábor Koplányi and Gergő Gyulai.

This research was performed within the frame of the OTKA grants K 128410 and K143571 from the National Research, Development and Innovation Office (NRDI) and funded by the National Research, Development, and Innovation Fund of Hungary under Grants TKP2021-EGA-02. S. Farah is grateful to the Stipendium Hungaricum scholarship program, the Ministry of Higher Education and Research Sudan as well as University of Khartoum, Sudan for their financial support. B. Gyarmati acknowledges the János Bolyai Research Scholarship of the Hungarian Academy of Sciences

Appendix A. Supplementary data

Supplementary data to this article can be found online at https://doi.org/10.1016/j.molliq.2023.122451.

References

[1] W.S. Hummers Jr., R.E. Offeman, Preparation of graphitic oxide, J. Am. Chem. Soc. 80 (1958) 1339, https://doi.org/10.1021/ja01539a017.
[2] B.C. Brodie, On the atomic weight of graphite, Philos. Trans. R Soc. London. 149 (1859) 249–259.
[3] L. Staudenmaier, Verfahren zur Darstellung der Graphitsäure, Ber. Dtsch. Chem. Ges. 31 (1898) 1481–1487.
[4] D.C. Marcano, D.V. Kosynkin, J.M. Berlin, A. Sinitskii, Z. Sun, A. Slesarev, et al., Improved synthesis of graphene oxide, ACS Nano 4 (2010) 4806–4814, https://doi.org/10.1021/nn1006368.
[5] A. Bianco, H.-M. Cheng, T. Enoki, Y. Gogotsi, R.H. Hurt, N. Koratkar, T. Kyotani, M. Monthioux, C.R. Park, J.M.D. Tascón, J. Zhang, All in the graphene family – A recommended nomenclature for two-dimensional carbon materials, Carbon 65 (2013) 1–6, https://doi.org/10.1016/j.carbon.2013.08.038.
[6] C. Botas, P. Álvarez, C. Blanco, R. Santamaría, M. Granda, P. Ares, F. Rodríguez-Reinoso, R. Menéndez, The effect of the parent graphite on the structure of graphene oxide, Carbon 50 (2012) 275–282, https://doi.org/10.1016/j.carbon.2011.08.045.
[7] S.S. Shojaeenezhad, M. Farbod, I. Kazeminezhad, Effects of initial graphite particle size and shape on oxidation time in graphene oxide prepared by Hummers' method, J. Sci. Adv. Mater. Devices 2 (2017) 470–475, https://doi.org/10.1016/j.jsamd.2017.09.003.
[8] C.K. Chua, Z. Sofer, M. Pumera, Graphite oxides: Effects of permanganate and chlorate oxidants on the oxygen composition, Chem. Eur. J. 18 (2012) 13453–13459, https://doi.org/10.1002/chem.201202320.
[9] X. Wang, H. Bai, G. Shi, size fractionation of graphene oxide sheets by pH-assisted selective sedimentation, J. Am. Chem. Soc. 133 (2011) 6338–6342, https://doi.org/10.1021/ja200218y.
[10] J. Chen, Y. Li, L. Huang, N. Jia, C. Li, G. Shi, Size fractionation of graphene oxide sheets via filtration through track-etched membranes, Adv. Mater. 27 (2015) 3654–3660, https://doi.org/10.1002/adma.201501271.
[11] W. Zhang, X. Zou, H. Li, J. Hou, J. Zhao, J. Lan, B. Feng, S. Liu, Size fractionation of graphene oxide sheets by the polar solvent-selective natural deposition method, RSC Adv. 5 (2015) 146, https://doi.org/10.1039/C4RA08516G.
[12] U. Kim, K. Choi, K.H. Park, J. Lee, Y. Choi, J. Seo, N.K. Oh, S. Jung, H. Yang, J. H. Lee, C. Yang, H. Park, Size fractionation of graphene oxide via solvent-mediated consecutive charge manipulation and investigation of the size effect as hole transporting layer in perovskite solar cells, Chem. Nano Mat. 5 (2019) 776–783, https://doi.org/10.1002/cnma.201900133.
[13] H.V. Kumar, S.J. Woltornist, D.H. Adamson, Fractionation and characterization of graphene oxide by oxidation extent through emulsion stabilization, Carbon 98 (2016) 491–495, https://doi.org/10.1016/j.carbon.2015.10.083.
[14] H. Geng, B. Yao, J. Zhou, K. Liu, G. Bai, W. Li, Y. Song, G. Shi, M. Doi, J. Wang, Size fractionation of graphene oxide nanosheets via controlled directional freezing, J. Am. Chem. Soc. 139 (2017) 12517–12523, https://doi.org/10.1021/jacs.7b05490.
[15] L. Zhu, R. Liu, Z. Fang, P.O. Agboola, N.F. Al-Khalli, I. Shakir, Y. Xu, Efficient fractionation of graphene oxide based on reversible adsorption of polymer and size-dependent sodium ion storage, ACS Appl. Mater. Interfaces 11 (2019) 2218–2224, https://doi.org/10.1021/acsami.8b16188.
[16] H. Badenhorst, Microstructure of natural graphite flakes revealed by oxidation: Limitations of XRD and Raman techniques for crystallinity estimates, Carbon 6 (2014) 674–690, https://doi.org/10.1016/j.carbon.2013.09.065.
[17] A. Lerf, H. He, M. Forster, J. Klinowski, Structure of graphite oxide revisited‖, J. Phys. Chem. B 102 (23) (1998) 4477–4482, https://doi.org/10.1021/jp9731821.
[18] T. Szabó, O. Berkesi, P. Forgó, K. Josepovits, Y. Sanakis, D. Petridis, I. Dékány, Evolution of surface functional groups in a series of progressively oxidized graphite oxides, Chem. Mater. 18 (11) (2006) 2740–2749, https://doi.org/10.1021/cm060258±.
[19] Q. Luo, C. Wirth, E. Pentzer, Efficient sizing of single layer graphene oxide with optical microscopy under ambient conditions, Carbon 157 (2020) 395–401, https://doi.org/10.1016/j.carbon.2019.10.047.
[20] J. Chen, Y. Zhang, M. Zhang, B. Yao, Y. Li, L. Huang, C. Li, G. Shi, Water-enhanced oxidation of graphite to graphene oxide with controlled species of oxygenated groups, Chem. Sci. 7 (1874) 2016, https://doi.org/10.1039/C5SC03828F.
[21] L. Zhang, J. Liang, Y. Huang, Y. Ma, Y. Wang, Y. Chen, Size-controlled synthesis of graphene oxide sheets on a large scale using chemical exfoliation, Carbon 47 (2009) 3365–3380, https://doi.org/10.1016/j.carbon.2009.07.045.
[22] S.X. Qi, T. Zhou, S. Deng, G. Zong, X. Yao, Q. Fu, Size-specified graphene oxide sheets: ultrasonication assisted preparation and characterization, J. Mater. Sci. 49 (2014) 1785–1793, https://doi.org/10.1007/s10853-013-7866-8.
[23] Y. Si, E.T. Samulski, Synthesis of water soluble graphene, Nano Lett. 8 (2008) 1679–1682, https://doi.org/10.1021/nl080604h.
[24] S. Ryu, B. Lee, S. Hong, S. Jin, S. Park, S.H. Hong, H. Lee, Salting-out as a scalable, in-series purification method of graphene oxides from microsheets to quantum dots, Carbon 63 (2013) 45–53, https://doi.org/10.1016/j.carbon.2013.06.037.
[25] S. Kim, J. Lee, S.-S. Lee, Fractionation of graphene oxides by size selective adhesion with spherical particles, Macromol. Res. 24 (2016) 1098–1104, https://doi.org/10.1007/s13233-016-4146-x.
[26] J. Zhao, G. Chen, W. Zhang, P. Li, L. Wang, Q. Yue, H. Wang, R. Dong, X. Yan, J. Liu, High-resolution separation of graphene oxide by capillary electrophoresis, Anal. Chem. 83 (2011) 9100–9106, https://doi.org/10.1021/ac202136n.
[27] Y. Liu, D. Zhang, S. Pang, Y. Liu, Shang Size separation of graphene oxide using preparative free-flow electrophoresis, J. Sep. Sci. 38 (2015) 157–163, https://doi.org/10.1002/jssc.201401000.
[28] C. Cui, J. Huang, J. Huang, G. Chen, Size separation of mechanically exfoliated graphene sheets by electrophoresis, Electrochim. Acta 258 (2017) 793–799, https://doi.org/10.1016/j.electacta.2017.11.128.
[29] M. Davardoostmanesh, E.K. Goharshadi, H. Ahmadzadeh, Electrophoretic size fractionation of graphene oxide nanosheets, New J. Chem. 43 (2019) 5047, https://doi.org/10.1039/C8NJ06411C.
[30] H. Yue, W. Wei, Z. Yue, B. Wang, N. Luo, Y. Gao, D. Ma, G. Ma, Z. Su, The role of the lateral dimension of graphene oxide in the regulation of cellular responses, Biomaterials 33 (2012) 4013–4021, https://doi.org/10.1016/j.biomaterials.2012.02.021.
[31] T. Szabo, P. Maroni, I. Szilagyi, Size-dependent aggregation of graphene oxide, Carbon 160 (2020) 145–155, https://doi.org/10.1016/j.carbon.2020.01.022.
[32] B. Elham, S. Adrian, A. Abbas, F. Qiang, Q.G. Greg, S. Alastair, D.E. Dave, Fractionation of graphene oxide single nano-sheets in water-glycerol solutions using gradient centrifugation, Carbon 103 (2016) 363–371, https://doi.org/10.1016/j.carbon.2016.02.095.
[33] S. Xiaoming, L. Zhuang, W. Kevin, R. Joshua Tucker, G. Andrew, Z. Sasa, D. Hongjie, Nano-graphene oxide for cellular imaging and drug delivery, Nano Res 1 (2008) 203–212, https://doi.org/10.1007/s12274-008-8021-8.
[34] X. Sun, D. Luo, J. Liu, D.G. Evans, Monodisperse chemically modified graphene obtained by density gradient ultracentrifugal rate separation, ACS Nano 4 (2010) 3381–3389, https://doi.org/10.1021/nn1000386.
[35] U. Khan, A. O'Neill, H. Porwal, P. May, K. Nawaz, J.N. Coleman, Size selection of dispersed, exfoliated graphene flakes by controlled centrifugation, Carbon 50 (2012) 470–475, https://doi.org/10.1016/j.carbon.2011.09.001.
[36] A.A. Green, M.C. Hersam, Solution phase production of graphene with controlled thickness via density differentiation, Nano Lett. 9 (2009) 4031–4036, https://doi.org/10.1021/nl902200b.
[37] T. Zhang, D. Zhang, M. Shen, A low-cost method for preliminary separation of reduced graphene oxide nanosheets, Mater. Lett. 63 (2009) 2051–2054, https://doi.org/10.1016/j.matlet.2009.06.050.
[38] G.G. Stokes, On the effect of the internal friction of fluids on the motion of pendulums, Trans Cambridge Philos Soc. (1850,) 8–106.
[39] C. Ambler, Theory of Centrifugation, Ind. Eng. Chem. 53 (1961) 430–433, https://doi.org/10.1021/ie50618a022.
[40] W.H. Bragg, W.L. Bragg, The reflexion of X-rays by crystals, Proc. R. Soc. Lond. A 88 (1913) 428–438, https://doi.org/10.1098/rspa.1913.0040.
[41] P. Scherrer, Bestimmung der Größe und der inneren Struktur von Kolloidteilchen mittels Röntgenstrahlen, Göttinger Nachrichten Math. Phys. 2 (1918) 98–100.
[42] J.I. Langford, A.J.C. Wilson, Scherrer after Sixty Years: A survey and some new results in the determination of crystallite size, J. Appl. Crystallogr. 11 (1978) 102–113, https://doi.org/10.1107/s0021889878012844.
[43] L.G. Cançado, K. Takai, T. Enoki, General equation for the determination of the crystallite size La of nanographite by Raman spectroscopy, Appl. Phys. Lett. 88 (2006), 163106, https://doi.org/10.1063/1.2196057.
[44] H.D. Everett, Reporting data on adsorption from solution at the solid/solution interface, Pure Appl. Chem. 58 (1986) 967–984, https://doi.org/10.1351/pac198658070967.
[45] J. Jagiello, T.J. Bandosz, J.A. Schwarz, Carbon surface characterization in terms of its acidity constant distribution, Carbon 32 (1994) 1026–1028, https://doi.org/10.1016/0008-6223(94)90066-3.
[46] J. Jagiello, Stable numerical solution of the adsorption integral equation using splines, Langmuir 10 (1994) 2778–2785, https://doi.org/10.1021/la00020a045.

[47] G. Gyulai, F. Ouanzi, I. Bertóti, M. Mohai, T. Kolonits, K. Horváti, S. Bősze, Chemical structure and in vitro cellular uptake of luminescent carbon quantum dots prepared by solvothermal and microwave assisted techniques, J. Colloid Interface Sci. 549 (2019) 150–161, https://doi.org/10.1016/j.jcis.2019.04.058.
[48] V. Schmiedova, J. Pospisil, A. Kovalenko, P. Ashcheulov, L. Fekete, T. Cubon, P. Kotrusz, O. Zmeskal, M. Weite, Physical properties investigation of reduced graphene oxide thin films prepared by material inkjet printing, J. Nanomater. (2017), https://doi.org/10.1155/2017/3501903.
[49] B. Gyarmati, S. Farah, A. Farkas, G. Sáfrán, L.M. Voelker-Pop, K. László, Long-term aging of concentrated aqueous graphene oxide suspensions seen by rheology and Raman spectroscopy, Nanomaterials 12 (2022) 916, https://doi.org/10.3390/nano12060916.
[50] D.H. Everett, Basic principles of colloid science, Royal Society of Chemistry, London, 1988. Chapters 3 and 8.
[51] J. Amaro-Gahete, A. Benítez, R. Otero, D. Esquivel, C. Jiménez-Sanchidrián, J. Morales, Á. Caballero, F.J. Romero-Salguero, A comparative study of particle size distribution of graphene nanosheets synthesized by an ultrasound-assisted method, Nanomaterials 9 (2019,152.), https://doi.org/10.3390/nano9020152.
[52] L. Vannozzi, E. Catalano, M. Telkhozhayeva, E. Teblum, A. Yarmolenko, E. S. Avraham, R. Konar, G.D. Nessim, L. Ricotti, Graphene oxide and reduced graphene oxide nanoflakes coated with glycol chitosan, propylene glycol alginate, and polydopamine: Characterization and cytotoxicity in human chondrocytes, Nanomaterials 11 (2021) 2105, https://doi.org/10.3390/nano11082105.
[53] A. Lerf, A. Buchsteiner, J. Pieper, S. Schöttl, I. Dekany, T. Szabo, H.P. Boehm, Hydration behavior and dynamics of water molecules in graphite oxide, J. Phys. 9999Chem. Solids 67 (2006) 1106–1110, https://doi.org/10.1016/j.jpcs.2006.01.031.
[54] A. Paudics, S. Farah, I. Bertóti, A. Farkas, K. László, M. Mohai, G. Sáfrán, A. Szilágyi, M. Kubinyi, Fluorescence probing of binding sites on graphene oxide nanosheets with Oxazine 1 dye, Appl. Surface Sci. 541 (2021), 148451, https://doi.org/10.1016/j.apsusc.2020.148451.
[55] S. Claramunt, A. Varea, D. López-Díaz, M.M. Velázquez, A. Cornet, A. Cirera, The importance of interbands on the interpretation of the Raman spectrum of graphene oxide, J. Phys. Chem. C 119 (2015) 10123–10129, https://doi.org/10.1021/acs.jpcc.5b01590.
[56] O. Akhavan, Bacteriorhodopsin as a superior substitute for hydrazine in chemical reduction of single-layer graphene oxide sheets, Carbon 81 (2015) 158–166, https://doi.org/10.1016/j.carbon.2014.09.044.
[57] D. López-Díaz, M.L. Holgado, J.L. García-Fierro, M.M. Velázquez, Evolution of the Raman spectrum with the chemical composition of graphene oxide, J. Phys. Chem. C 121 (2017) 20489–20490, https://doi.org/10.1021/acs.jpcc.7b06236.
[58] A. Cuesta, P. Dhamelincourt, J. Laureyns, A. Martínez-Alonso, J.M.D. Tascón, Raman microprobe studies on carbon materials, Carbon 32 (1994) 1523–1532, https://doi.org/10.1016/0008-6223(94)90148-1.
[59] D. Yin, N. Lu, Z.-Y. Li, J.-L. Yang, A computational infrared spectroscopic study of graphene oxide, J. Chem. Phys. 139 (2013), 084704, https://doi.org/10.1063/1.4818539.
[60] X. Jiao, Y. Qiu, L. Zhangab, X. Zhang, Comparison of the characteristic properties of reduced graphene oxides synthesized from natural graphites with different graphitization degrees, RSC Adv. 7 (2017) 52337–52344, https://doi.org/10.1039/C7RA10809E.
[61] J. Zhao, S. Pei, W. Ren, L. Gao, H.-M. Cheng, Efficient preparation of large-area graphene oxide sheets for transparent conductive films, ACS Nano 4 (2010) 5245–5252, https://doi.org/10.1021/nn1015506.
[62] S. Stankovich, D.A. Dikin, R.D. Piner, K.A. Kohlhaas, A. Kleinhammes, Y. Jia, Y. Wu, S.B.T. Nguyen, R.S. Ruoff, Synthesis of graphene-based nanosheets via chemical reduction of exfoliated graphite oxide, Carbon 45 (2007) 1558–1565, https://doi.org/10.1016/j.carbon.2007.02.034.
[63] E. Aliyev, V. Filiz, M.M. Khan, Y.J. Lee, C. Abetz, V. Abetz, Structural characterization of graphene oxide: Surface functional groups and fractionated oxidative debris, Nanomaterials 9 (2019) 1180, https://doi.org/10.3390/nano9081180.
[64] J. Mewis, N.J. Wagner, Colloidal Suspension Rheology, Cambridge University Press, Cambridge, UK, 2012.
[65] B. Konkena, S. Vasudevan, Glass, gel, and liquid crystals: Arrested states of graphene oxide aqueous dispersions, J. Phys. Chem. C. 118 (2014) 21706–21713, https://doi.org/10.1021/jp507266t.
[66] S. Naficy, R. Jalili, S.H. Aboutalebi III, R.A. Gorkin, K. Konstantinov, P.C. Innis, G. M. Spinks, P. Poulin, G.G. Wallace, Graphene oxide dispersions: Tuning rheology to enable fabrication, Mater. Horiz. 1 (2014) 326–331, https://doi.org/10.1039/C3MH00144J.
[67] P. Kumar, U.N. Maiti, K.E. Lee, S.O. Kim, Rheological properties of graphene oxide liquid crystal, Carbon 80 (2014) 453–461, https://doi.org/10.1016/j.carbon.2014.08.085.
[68] Z. Xu, C. Gao, Aqueous liquid crystals of graphene oxide, ACS Nano 5 (2011) 2908–2915, https://doi.org/10.1021/nn200069w.
[69] H. Bai, C. Li, X. Wang, G. Shi, On the gelation of graphene oxide, J. Phys. Chem. C 115 (2011) 5545–5551, https://doi.org/10.1021/jp1120299.